ACS APPLIED MATERIALS & INTERFACES

Surfaces, Interfaces, and Applications

Emergent ferroelectricity in otherwise non-ferroelectric oxides by oxygen vacancy design at heterointerfaces

Ri He, Junliang Lin, Qing Liu, Zhaoliang Liao, Lingling Shui, Zhan Jie Wang, Zhicheng Zhong, and Run-Wei Li

ACS Appl. Mater. Interfaces, **Just Accepted Manuscript** • DOI: 10.1021/acsami.0c13314 • Publication Date (Web): 15 Sep 2020

Just Accepted

is published by the American Chemical Society. 1155 Sixteenth Street N.W., Washington, DC 20036

Emergent ferroelectricity in otherwise non-ferroelectric oxides by oxygen vacancy design at heterointerfaces

Ri He,[1,2,6‡] *Jun Liang Lin*,[3,4‡] *Qing Liu*,[1] *Zhaoliang Liao*,[5*] *Lingling Shui*,[2] *Zhan Jie Wang*,[7*] *Zhicheng Zhong*,[1,8*] *Run-Wei Li*,[1,8]

[1]*Key Laboratory of Magnetic Materials Devices & Zhejiang Province Key Laboratory of Magnetic Materials and Application Technology, Ningbo Institute of Materials Technology and Engineering, Chinese Academy of Sciences, Ningbo 315201, China.*

[2]*School of Information and Optoelectronic Science and Engineering, South China Normal University, Guangzhou 510006, China.*

[3] *College of Light Industry, Liaoning University, Shenyang 110036, China.*

[4] *School of Materials Science and Engineering, Northeastern University, Shenyang 110819, China.*

[5]*National Synchrotron Radiation Laboratory, University of Science and Technology of China, Hefei 230026, China.*

[6]*International Academy of Optoelectronics at Zhaoqing, South China Normal University, Zhaoqing 526238, China.*

[7]*School of Materials Science and Engineering, Shenyang University of Technology, Shenyang 110870, China.*

[8]*China Center of Materials Science and Optoelectronics Engineering, University of Chinese Academy of Sciences, Beijing 100049, China.*

**Corresponding* authors:

E-mail address: Zhaoliang Liao(zliao@ustc.edu.cn); Zhicheng Zhong (zhong@nimte.ac.cn); Zhan Jie Wang(wangzj@imr.ac.cn)

‡ These authors contributed equally to this work.

Abstract

Introducing point defects in complex metal oxides is a very effective route to engineer crystal symmetry and thereby control physical properties. However, the inversion symmetry breaking, which is vital for many tantalizing properties, such as ferroelectricity and chiral spin structure, is usually hard to be induced in bulk crystal by point defects. By designing oxygen vacancies formation energy profile and migration path across oxide heterostructure, our first principles density functional theory (DFT) calculations demonstrate that the point defects can effectively break the inversion symmetry and hence to create novel ferroelectricity in superlattices comprised of otherwise non-ferroelectric materials $SrTiO_3$ and $SrRuO_3$. This induced ferroelectricity can be significantly enhanced by reducing $SrTiO_3$ thickness. Inspired by theory calculation, $SrTiO_3$/$SrRuO_3$ superlattices were experimentally fabricated and are found to exhibit surprising strong ferroelectric properties. Our finding paves a simple and effective pathway to engineer the inversion symmetry and thus properties by point defect control in oxide heterostructures.

KEYWORDS: *oxygen vacancies*, *inversion symmetry breaking*, *ferroelectric polarization*, *oxides*

heterostructures, *perovskite*, *first-principles*

1. Introduction

Defects which are ubiquitous in crystal materials afford one of the most important twists to tip delicate interaction between the spin, charge, orbital, and lattice degrees-of-freedom, thus to optimize desired properties and to create new matter of states.[1-4] Numerous properties and functionalities are found to be intimately correlated to the defects, producing a fertile playground for many advanced applications. In terms of microscale, defects are well-known to have a profound influence on electronic structure of a material. For instance, the extrinsic dopants in a covalently bonded semiconducting material can tune charge carrier concentration and band gap.[5, 6] In ionically bonded complex transition metal oxides, which exhibit a variety of electronic phases and exotic properties, defects can go beyond the simple change of carrier concentration to create new electronic phase and to induce phase transition. Examples include dopant driven high-temperature superconductivity of copper oxides,[7-9] colossal magneto-resistance of manganese oxides,[10, 11] and metal to insulator transition in rare-earth perovskite $RNiO_3$.[12-14]

Another significant consequence of introducing defects is the macroscopic impact on the crystal symmetry. In particular, the translational symmetry is broken and the residual point symmetry might be reduced as well. As a result, the symmetry of this defect is characterized instead by a subgroup of its original point group.[15, 16] Given that the most prominent properties of any solid crystal lie in its symmetry, e.g., magnetism and superconductivity due to broken time-reversal symmetry,[17-19] spontaneous electric polarization, Rashba spin splitting and Dzyaloshinskii–Moriya interaction resulting from breaking spatial inversion symmetry,[20-23] it is highly expected to achieve novel phases by defect engineered symmetry. Regarding the point defects in complex metal oxides, they are not able to break the inversion symmetry in most situations.[15] Taking bulk $SrTiO_3$ (STO) as an example, introducing an isolated oxygen vacancy does not change the inversion symmetry of crystal (Figure 1a). Therefore, many broken inversion symmetry driven emergent properties are inhibited in bulk materials

according to Neumann's principle, said that the symmetry elements of any physical property of a crystal must include the symmetry elements of the point group of the crystal.[24] Fortunately, such situation can be completely altered at interface between two iso-structured materials where inversion symmetry is naturally broken. As illustrated in Figure 1b, the inversion symmetry of an isolated oxygen vacancy can be compositionally broken, in strong contrast to the conservation of inversion symmetry in bulk crystal as shown in Figure 1a. The point defects-controlled inversion symmetry breaking and thereby emergent properties can be anticipated in oxide heterostructures. Thanks to the advanced modern thin-film epitaxy techniques,[25, 26] atomic-level synthesis and control of complex oxide heterostructures become feasible.[27] Therefore, it is worth to cultivate novel physical effects driven by point defects in oxide heterostructures.

In ABO_3 perovskite oxide heterostructures, point defects can occupy different atomic sites, which will impose different impacts on crystal symmetry, e.g., oxygen vacancy in BO_2 layer vs. oxygen vacancy in AO layer at interfaces.[28] To achieve desired properties usually requires a well control of oxygen vacancy occupying a desired atomic site.[29, 30] Furthermore, the as-grown sample will experience a high temperature thermodynamics process during growth, which favors disordering defect structures.[31] To obtain significant point defect driven symmetry breaking and as a result to induce novel properties, a delicate interface where point defects can be well controlled at specific sites is highly desired. In this letter, we conceptually demonstrate a creation of pronounced ferroelectricity in an artificially designed $SrTiO_3/SrRuO_3$ (STO/SRO) superlattice by finely tuning the oxygen vacancy structure at interface using density functional theory (DFT) calculations together with kinetic Monte Carlo (KMC) simulations and Landau Ginzburg-Devonshire (LDG) phenomenological theory. Inspired by the theory analysis, surprised ferroelectric properties have been realized experimentally in STO/SRO superlattices grown by pulsed laser deposition. Our results provide a new twist toward novel functionalities in oxide heterostructures by defect-engineered symmetry breaking.

2. Methods

2.1. First-principles Density Functional Theory (DFT) calculations.

For bulk STO and $(STO)_9/(SRO)_1$ superlattices, 1×1×10 supercell containing 50 atoms (49 atoms for supercell with single oxygen vacancy) was used. The in-plane lattice constants of supercells were fixed at 3.907 Å, which correspond to the optimized calculated value of cubic STO. An isolated oxygen vacancy was added in the SrO, TiO and RuO layers for $(STO)_9/(SRO)_1$ superlattices. All internal atomic positions were allowed to fully relax. The DFT calculations were performed using a plane-wave basis set with a cutoff energy of 500 eV as implemented in the Vienna *ab initio* simulation package (VASP),[32, 33] and electron exchange-correlation potential was described using generalized gradient approximation and Perdew-Burke-Ernzerhof solid scheme.[34] The Brillouin zone was sampled with a 12 × 12 × 1 Monkhorst-Pack k-point grid. We chose formation energy of an oxygen vacancy in bulk STO as a reference state for our calculations of formation energy of a single oxygen vacancy (E^{Vo}) in $(STO)_9/(SRO)_1$ superlattices, i.e. $E^{Vo} = E^{Vo}_{STO/SRO} - E^{Vo}_{STO}$. The formation energy of different arrangements of divacancies in the interface were taken into account using a $\sqrt{2} \times \sqrt{2}$ ×10 $(STO)_9/(SRO)_1$ supercells with the in-plane lattice constant fixed to the calculated lattice constant of STO. After full atomic relaxation, considering all positive and negative charge sites, the local unit cells polarization could be calculated by atomic displacements with respect to the referenced cubic phase multiplied by the Born effective charges of cubic STO. The components of Born effective charge tensors along *z* axis (out-of-plane direction) were obtained by the DFT calculations: Z_{Sr}= 2.54, Z_{Ti} = 7.12, Z_{O1} = −5.66, Z_{O2} = −2.00, O1 denotes the oxygen atom at the SrO layer (apical oxygen), and O2 denotes the oxygen atom at the TiO_2 layer.

2.2. Kinetic Monte Carlo (KMC) method.

Kinetic Monte Carlo (KMC) method has been proven to be very effective in the investigation of oxygen atoms diffusion and interaction in complex oxides. A STO/SRO superlattice was considered in this model with two metal electrodes for

applying bias. The oxygen atoms form a pseudo-cubic lattice and are trapped in the SRO region as illustrated below. Every oxygen vacancy can diffuse through two major diffusion paths-(i) oxygen vacancy diffusion in the SRO and (ii) diffusion along the interfaces. The corresponding diffusion barriers without voltage bias are denoted as H_{SRO} and H_{int}. Without bias, the vacancy diffusion coefficient (i.e. hopping rate) can be evaluated by $D_V = D_V^0 \exp(-H/kT)$, where H represents diffusion barrier, k is the Boltzmann constant and T is the temperature. D_V^0 is the constant which is fixed to a typical value of 1×10^{12}/s. In this simulation, E_{SRO} and E_{int} were fixed to 0.9 eV and 0.6 eV, respectively. When voltage bias was applied along z axis, the diffusion barriers will be modified along z axis: $D_V = D_V^0 \exp[-(H-E_{bias})/kT]$. Here, E_{bias} is the reduced energy barrier caused by the external bias.[35, 36] The initial configuration was set as an $(STO)_9/(SRO)_1$ superlattice comprised of 30×30×40 unit cells with 1800 oxygen vacancies randomly distributed at six symmetrical STO/SRO interfaces.

2.3. Landau Ginzburg-Devonshire (LGD) phenomenological approach

The Landau Ginzburg-Devonshire (LGD) phenomenological theory approach calculation was used to model polarization upon external electric field in the $(STO)_9/(SRO)_1$ superlattices. The LGD phenomenological calculation is performed with assumption that oxygen vacancy induced elastic dipoles can be transformed into electric dipoles due to the bond breaking and lattice distortion in superlattices. The dynamics of the polarization upon a periodic external electric field $E(t)=E_0 sin(\omega t)$ follows the relaxation time-dependent equation that proposed by Ref. [37]:

$$\frac{\partial P}{\partial t} = \frac{\delta G}{\delta P} \approx\ll \alpha_{33}^R \gg P + \beta P^3 + \gamma P^5 - E(t) \qquad (1)$$

where P is polarization, G is Gibbs free energy density of superlattices, α^R_{33}, β and γ is LGD-expansion coefficients that related to the temperature, thickness of films and concentration of oxygen vacancies, respectively (for detail see Ref. [37]). In this model, the elementary polarization from the elastic dipole was input from DFT calculation. The thickness of films was set to 10 unit cell and the concentration of oxygen vacancies range from 1 to 0.

2.4. Film Growth and Characterizations

$(STO)_9/(SRO)_1$ superlattice was grown on (001) 0.7wt% Nb doped $SrTiO_3$ substrates by pulsed laser deposition (PLD) using a KrF excimer laser operating at $\lambda = 248$ nm. The laser energy density and repetition rate were 1.3 J/cm^2 and 5 Hz, respectively. The temperature during growth is maintained at 650 ^oC and the oxygen partial pressure is 20 Pa. Total thickness of the film is ~ 250 nm. The ferroelectric P-E hysteresis loops were measured at 1 kHz using a standard ferroelectric testing system (TF2000E; Aixacct, Aachen, Germany). Considering STO crystals undergo a cubic to tetragonal phase transition at ~105 K,[38] all the measurements were performed at room temperature to ensure the STO has pure cubic phase under ideal conditions.

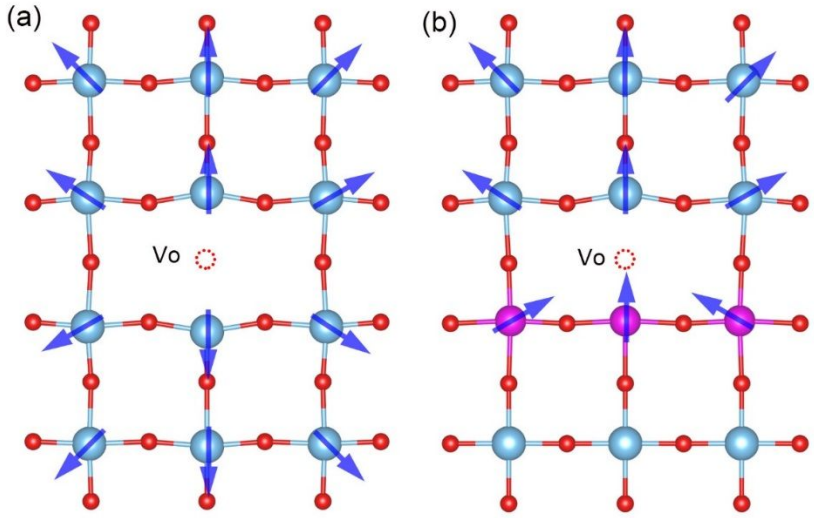

Figure 1. (a) Schematic plot of the local polarization patterns for oxygen vacancy configuration in bulk STO and (b) STO/SRO heterointerface. Red, blue and purple spheres represent O, Ti and Ru atoms, and the oxygen vacancy is marked by a red dotted circle. The Sr atoms are not presented. Blue arrows indicate the atomic displacement with respect to the referenced vacancy-free configurations.

3. Results and Discussion

3.1. Oxygen Vacancy induced Polarization

The STO was chose as a prototype to investigate polarization because of its quantum paraelectric state and that it is a golden substrate widely used in condensed matter physics.[39, 40] At room temperature, STO crystallizes in a cubic perovskite structure with

O_h ($m3m$) symmetry ($Pm3m$ space group). Oxygen vacancies are very common in STO and very crucial for many properties, such as transport properties and magnetization.[31, 41-43] In infinite boundary bulk STO, introducing an oxygen vacancy although can break the inversion symmetry within local unit cell by cutting off the Ti-O bond and introducing local lattice distortion, but it cannot break the long-range inversion symmetry, as illustrated in Figure 1a. As a consequence, local unit cell can only manifest a series of specific spatial inversion symmetry breaking driven local spontaneous polarization, whereas the whole crystal does not exhibit long range polarization. To prove this hypothesis, we built a periodic 10 layers of STO supercell comprised of isolated oxygen vacancy in SrO layer and examined the atomic displacements of Ti , O, and Sr atoms by performing the DFT calculation. The atomic relaxation of the supercell is shown in Figure 2a. It is observed that Ti atoms shift off the center of pseudo-cubic unit cell, leading to tail-to-tail displacement pattern in the supercell. The Ti atom displacement is as large as 0.3 Å (Figure S1) and hence gives rise to a very pronounced local polarization of 45.6 μC/cm^2 in unit cells near the oxygen vacancy as shown in Figure 2c. However, such local polarization cannot produce a net polarization in long range due to formation of periodic tail-to-tail antipolar pattern as shown by blue arrows in Figure 2a. Such tail-to-tail polarization arises from the inversion symmetry of D_{4h} point group in STO supercell with isolated oxygen vacancy.

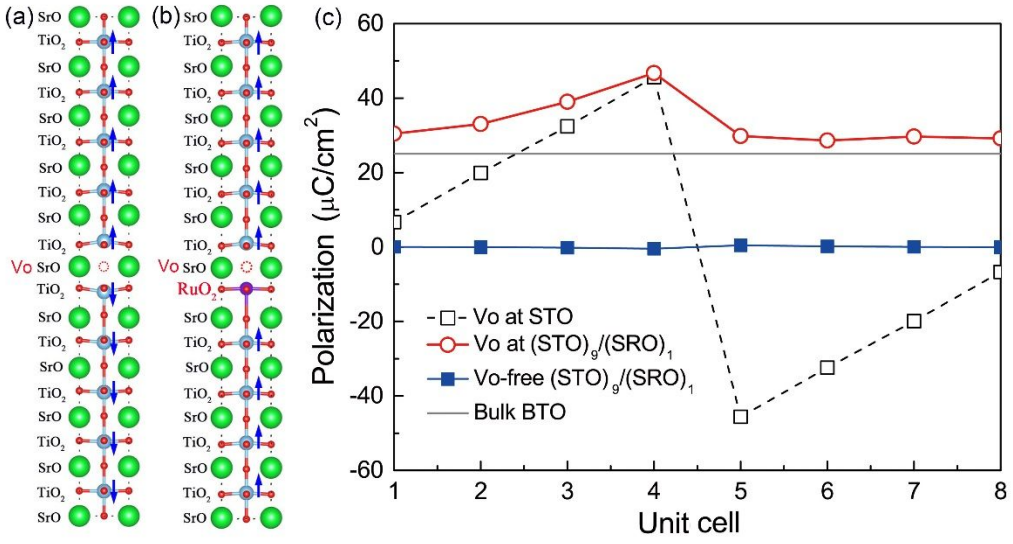

Figure 2. (a) The unit cell of bulk STO with an oxygen vacancy at SrO layer and (b) $(STO)_9/(SRO)_1$ superlattice with an oxygen vacancy (V_O) at the SrO interface. Blue arrows indicate the direction of off-centering of Ti atoms, and the direction of local polarization as well. (c) The profile of local spontaneous polarization. The black squares and red circles are polarization profiles for bulk STO with an V_O and superlattice an V_O, respectively. The polarization of defect-free bulk $BaTiO_3$ and superlattice is shown as a gray horizontal line and blue solid squares, respectively. The polarization was calculated using the computed Born effective charges.

In order to gain net macroscopic polarization in STO supercell, it is necessary to break the periodic tail-to-tail antipolar displacement pattern of Ti atoms (i.e. break the inversion symmetry). Aiming for this goal, another iso-structural material is chosen to interface the STO to form heterostructures. The $SrRuO_3$ (SRO), which is a well-known bad ferromagnetic metal and widely used for oxide electrode, is found to be an idea candidate to be stacked with STO to form SRO/STO interface.[44] The unique oxygen vacancies formation energy and diffusion barrier relative to STO can create synergetic effects of breaking inversion symmetry and favoring the preferred formation of oxygen vacancies at interface as illustrated below. Furthermore, SRO has a specific lattice distortion induced by oxygen vacancy: the oxygen vacancy cuts off the Ru-O bond in SRO, leading to the Ru atoms move forward to the site of oxygen vacancy rather than moving away from the oxygen vacancy in conventional perovskites. For SRO/STO superlattice, introducing oxygen vacancy defects at interface is found to change the point group from nonpolar D_{4h} group to polar C_{4v} group. In other words, the inversion symmetry is broken (see group theory analysis in Supporting Information and Table S1). We first investigated the atomic displacements of Ti, O, and Sr atoms in a periodic $(STO)_9/(SRO)_1$ supercell. In the case of oxygen-vacancy free supercell, our calculations show a negligible symmetrical polarization at interface as shown in Figure 2c. When an oxygen vacancy is introduced in the interfacial SrO layer, a head-to-tail polar displacement pattern is formed, in strong contrast to aforementioned tail-to-tail polar displacement pattern in defective STO supercell as shown in Figure 2a and Figure 2b. Such a periodic head-to-tail polarization leads to a net polarization of 33.3 $\mu C/cm^2$, which is larger than that of $BaTiO_3$ (=25.5 $\mu C/cm^2$).[45] It should be noted that polarization in nonpolar perovskite oxide heterostructures can be also induced by

lattice-mismatch-strain which has been reported from first-principles calculations and experiments[46-49]. For example, biaxial tensile strain can lead to an in-plane polarization of STO;[46] and biaxial compressive strain can lead to an out-of-plane polarization in nonpolar $CaZrO_3/SrTiO_3$ heterostructure.[47] In STO/SRO superlattice, SRO has a pseudocubic cell with a lattice parameter of 3.923Å.[44] This parameter is very close to the STO lattice parameter of 3.905Å, hence the STO may suffers only a small tensile strain of 0.41% at most. We examined the effect of epitaxial tensile strain by fixed the values of the lattice parameters to 3.923Å in superlattice models and found that 0.41% tensile strain has very minor effect on polarization in both superlattice models (Figure S2). This behavior can be easy to understood through coupling term $-(S_1 P_1^2 + S_2 P_2^2 + S_3 P_3^2)$ in Landau-like free-energy expansion, where P_i (i=1, 2, 3) denote the polarization along *x*, *y* and *z* axis, and S_i denote the Voigt notation of strain components.[50] For in-plane biaxial tensile strain, S_1 and $S_2 > 0$, but $S_3 < 0$, resulting the system lowers its energy by adopting the $P_3 = 0$ configuration.[49] Therefore, the strain induced polarization can be excluded in the model. Concentration of oxygen vacancy can affect the polarization property in superlattice. The concentration of oxygen vacancy in the superlattice in above calculation is 1. Here and after, the oxygen vacancy concentration is defined as the number of oxygen vacancy divided by original total oxygen atoms at interface. Given that oxygen vacancy concentration is relatively lower in real experimental samples,[51] several more different oxygen vacancy concentrations in the supercell are investigated theoretically to better simulate the real samples. The oxygen vacancy concentration of 0.5 and 0.25 in the supercells were adopted, respectively. It is observed that decreasing oxygen vacancy concentration leads to smaller net average polarization (Figure S3). However, the net polarization is still as large as 11.3 μC/cm^2 when the oxygen vacancy concentration is decreased from 1 to 0.25.

For conventional perovskite ferroelectric materials such as $BaTiO_3$, first principles calculation predicts a critical thickness of six unit cells owing to incomplete screening of depolarization field.[52] Indeed, many ferroelectric perovskite materials are

experimentally found to have a ferroelectric dead layer with thickness of about 1-5 nm.[53-57] With respect to this defect-driven ferroelectricity, our calculation surprisingly shows that decreasing the thickness of STO instead greatly enhances the polarization and at the same time stabilizes the polarization (Figure S4). This phenomenon is similar to that reported recently in doped HfO_2 where not only the ferroelectric critical thickness is absent but also polarization is enhanced as film thickness is reduced, unlike in conventional ferroelectrics.[58, 59] Interestingly, oxygen vacancies in ultrathin HfO_2 was also proposed as key mechanism to induce ferroelectric polarization by several studies.[37, 60, 61] This fact implies a possible enhancement of ferroelectricity at reduced dimensionality in ultrathin films. Furthermore, oxygen vacancy induced polarization could be widely applied in other non-polar dielectric materials in principle. For example, our calculation shows a net polarization of 11.43 μC/cm^2 in $(LaAlO_3)_9/(LaNiO_3)_1$ superlattice with oxygen vacancy at interface (Figure S5).

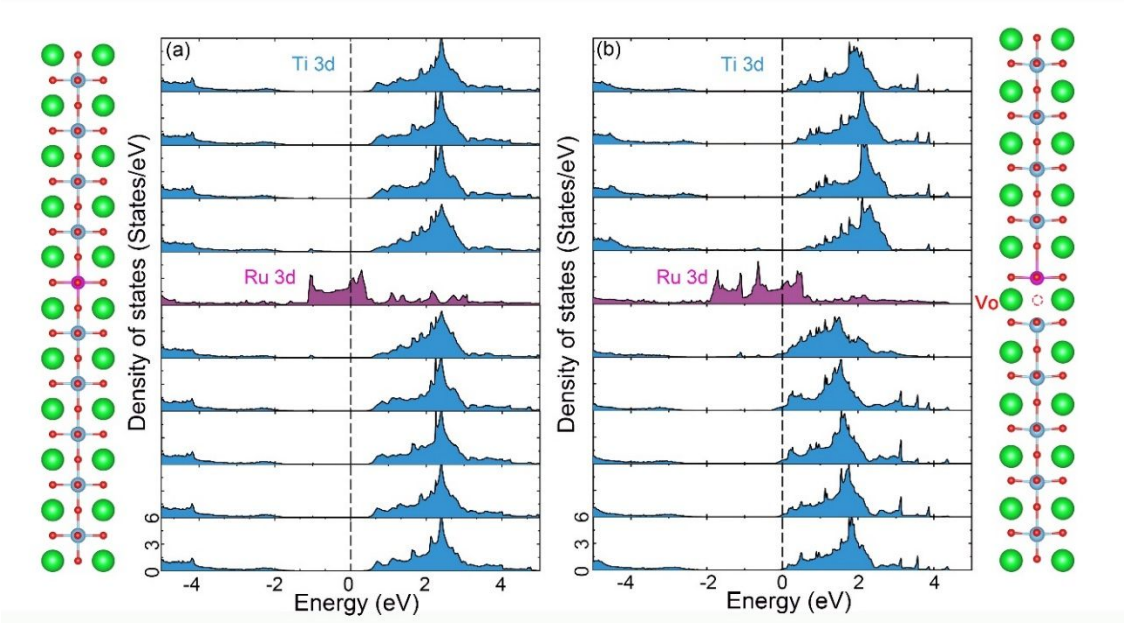

Figure 3. The structure of $(STO)_9/(SRO)_1$ superlattices and corresponding layer-resolved partial density of states (PDOS) projected on Ti *3d* and Ru *3d* orbitals with (a) and without oxygen vacancy (b).

When oxygen vacancies of high concentration are induced in perovskite oxide films,

the insulating oxides may undergo an insulator-metal transition and become conductive, which is in conflict with ferroelectricity.[62, 63] To identify the insulating of oxygen-deficient STO/SRO superlattice, we calculated the layer-resolved partial density of states (PDOS) projected on Ti 3*d* and Ru 3*d* orbitals. As shown in Figure 3a, we can observe no electron reconstruction at the interface region in the oxygen vacancy-free superlattice and the conduction bands are hovering above Fermi level at the TiO_2 layers, suggesting that the STO layers are insulating, similar to that of bulk STO. For the STO/SRO superlattices with high oxygen vacancy concentration at the interface, the PDOS plot in Figure 3b clearly reflects the presence of oxygen vacancy at the interface can induce interfacial electronic reconstruction. The Ti ions gain charges in the localized 3*d* states at the four sequential TiO_2 layers close to interface, and forming a slightly interfacial conductive state. However, the electron reconstruction subsides when at region away from the interfacial oxygen vacancy and the bulk insulating state is gradually recovered in subsequent STO layers.

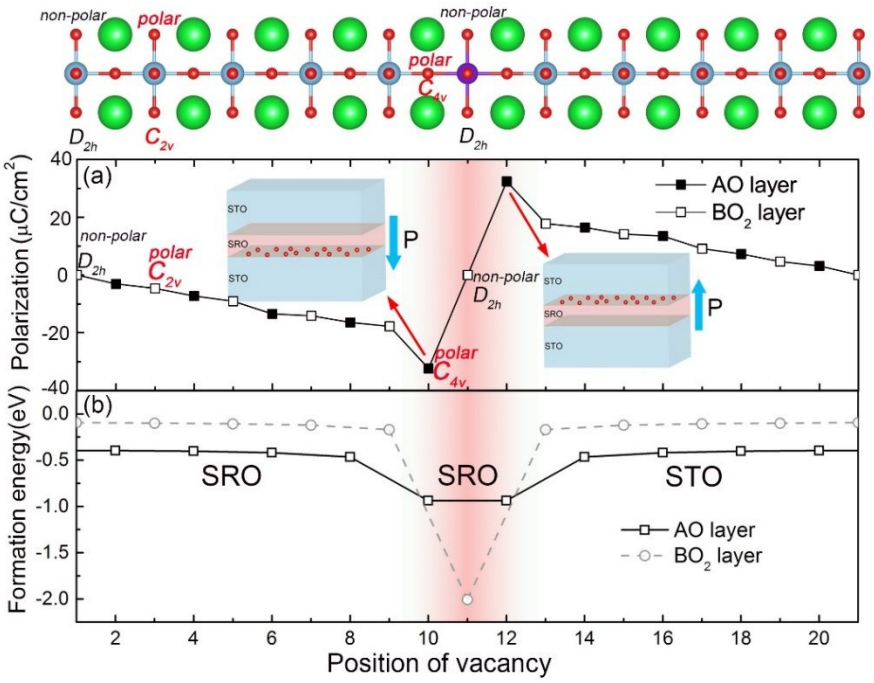

Figure 4. (a) Average net polarization of the $(STO)_9/(SRO)_1$ superlattice as a function of oxygen vacancy position in superlattice calculated from first principles with full-relaxation. Solid and hollow squares indicate oxygen vacancy in AO and BO_2 layers, respectively. Inset, down/up

polarization corresponding to oxygen vacancy located in SrO layer at bottom interface/top interface. Point group symbols of supercell with different oxygen vacancy sites are marked in corresponding positions. (b) Position dependence of the formation energy of an oxygen vacancy in a $(STO)_9/(SRO)_1$ superlattice relative to that of a vacancy in bulk STO.

3.2. The Effect of Oxygen Vacancy Sites on Symmetry

The atomic site of oxygen vacancy plays a vital role in affecting the crystal symmetry and polarization of supercells. When the oxygen vacancy migrates across heterostructure, the point group symmetry of the superlattice should be changed. Regarding the isolated oxygen vacancy in $(STO)_9/(SRO)_1$ supercell, the all possible oxygen vacancy sites can be divided into four groups based on its point group. As shown by crystal structure in Figure 4a, the oxygen vacancy in the leftmost TiO_2 layer (layer 1) and RuO_2 layer result in the point group of supercell is D_{2h}, which is a non-polar point group (note with a higher symmetry of 4/*mmm* in $(STO)_9/(SRO)_1$ supercell, the oxygen vacancies in layer 1 and layer 21 are equivalent, and the same for layer 2 and layer 20, 3 and 19, etc.). In contrast, the point group of supercells with oxygen vacancy in other TiO_2 layers (except the leftmost TiO_2 layer) and in SrO layers becomes polar point group of C_{2v} and C_{4v}, respectively, according to symmetry theory analysis (for detail, see Supporting Information). Therefore, it can be concluded that the polarization disappears as oxygen vacancy is located in the leftmost TiO_2 layer and RuO_2 layer, and is created as oxygen vacancy migrates to other TiO_2 layers and SrO layers. The polarization of the supercell as a function of oxygen vacancy sites is calculated by DFT and is shown in Figure 4a. In good agreement with symmetry theory analysis, polarization is formed in supercells with oxygen vacancy in the TiO_2 layers (except the leftmost TiO_2 layer) and RuO_2 layer, and disappears for oxygen vacancy in the leftmost TiO_2 layer and RuO_2 layer. Specifically, the superlattice with oxygen vacancy in the two interfacial SrO layers exhibits a maximum polarization and the polarization decreases as oxygen vacancy moves away from the interfacial SrO layer. What is more, it is found that the polarization is reversed when oxygen vacancy migrates from one SrO interface across the RuO_2 layer to a symmetrical neighboring SrO one. This fact suggests that polarization switching can be achieved if oxygen

vacancy site can be switched between these bi-stable configurations.

3.3. Formation Energy

Due to the crucial role of oxygen vacancy site for polarization, it is essential to investigate the site dependent formation energy of oxygen vacancy. Figure 4b shows the formation energies of single oxygen vacancy (E^{VO}) in $(STO)_9/(SRO)_1$ supercell. With a higher symmetry of D_{4h} (4/*mmm*) in $(STO)_9/(SRO)_1$ supercell, the E^{VO} is the same in symmetrically equivalent layers. The calculated E^{VO} profile indicates that the lowest E^{VO} for AO (SrO) occurs at the interfacial layers, whereas in BO_2 (RuO_2 and TiO_2) layers, the lowest E^{VO} occurs at the interfacial RuO_2 layer. We can conclude that the formation energy of interfacial SrO layer is obviously smaller than that in bulk STO region but larger than that in SRO region. Moreover, the interaction of divacancies should be considered.[64] The formation energy of possible arrangements of divacancies in supercell of $\sqrt{2} \times \sqrt{2}$ lattice in *xy*-plane is calculated. As shown in Figure S6, an oxygen-vacancy pair with one oxygen vacancy in interfacial SrO layer and the other one in interfacial RuO_2 layer, said interfacial SrO-RuO_2 oxygen vacancy pair, has the lowest E^{VO} than pairs with other configurations. This fact indicates that interfacial SrO-RuO_2 oxygen vacancy pair is more favorable. Such arrangement can generate nearly the same polarization of ~33 μC/cm^2 as single oxygen vacancy does as shown in Figure 2b.

According to DFT LDA + *U* calculations[41] and previous experiments,[65-68] oxygen diffusion in SRO is more difficult than that in STO, since the diffusion barrier of oxygen vacancy in bulk SRO is much higher (~0.9 eV) than that in STO (~0.6 eV). As a result, the oxygen vacancy tends to segregate at SRO due to its lower formation energy and then stop at two symmetrically interfacial SrO layers due to the high diffusion barrier in SRO. If the oxygen vacancy is distributed at two symmetrical interfaces, the opposite polarization at two interfaces will cancel each other and then cause a net zero polarization (Figure S7). This usually occurs for as-fabricated sample where thermodynamic process will cause random distribution of oxygen vacancy.[31] Since oxygen vacancy is positive charged species, in order to obtain long range polarization,

an electroforming process that moves oxygen vacancy to one interface as shown in Figure 2b is required. Electric field control of oxygen ions migration is the common strategy in tuning physical properties in complex oxide to produce extended functionalities.[69-72] To investigate the oxygen vacancy dynamics in SRO/STO superlattice, we use kinetic Monte Carlo (KMC) method to simulate the migration and interaction of oxygen vacancies in the STO/SRO superlattice under an external electric field (for detail see Methods). In this simulation, the initial configuration was set as an $(STO)_9/(SRO)_1$ superlattice of 30×30×40 unit cells with 1800 oxygen vacancies randomly distributed at six symmetrical STO/SRO interfaces, as depicted in Figure 5a. Figs. 5b and c show the final oxygen vacancy configurations under upward and downward out-of-plane electric field obtained from KMC simulations, respectively. It is found that no oxygen vacancy migration occurs when bias voltage is small than 0.1 V. When the voltage is increased to 0.2 V, a small number of vacancies hop along (001) direction across RuO_2 layer to neighboring interface. After the voltage is further increased to 0.8 V, all oxygen vacancies migrate to neighboring interface as shown in Figure 5b, leading to long-range polarization in superlattices according to aforementioned DFT calculation. When voltage is reversed to −0.8 V, all vacancies migrate back to previous neighboring interface as shown in Figure 5c, leading to reversion of long-range polarization. This fact implies that external electric-field controlled polarization switching is realistic. Furthermore, the field driven oxygen vacancies redistribution is stable due to higher diffusion barrier in SRO and lower formation energy at the interface than other regions. Therefore, the field induced polarization switching is non-volatile.

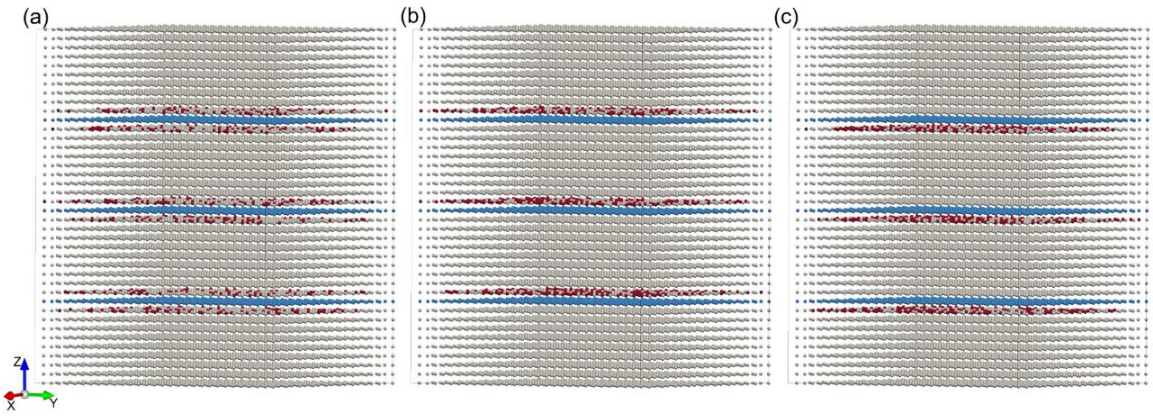

Figure 5. (a) Initial configuration of STO/SRO superlattice film of 30 × 30 ×40 unit cells with 1800 oxygen vacancies located at six interfaces between STO and SRO. The gray and blue spheres represent STO and SRO layers, respectively. Red spheres represent oxygen vacancies. Here, the electrodes are not presented. (b) The redistribution of oxygen vacancies at interface under upward out-of-plane electric field and (c) downward out-of-plane electric field obtained from KMC simulation.

3.4. Ferroelectric Simulation and Experiment

The Landau Ginzburg-Devonshire phenomenological theory were used to simulate the electric field dependent polarization in the $(STO)_9/(SRO)_1$ superlattices (for detail see Methods).[37] The concentration of the interfacial oxygen vacancy was varied from 0 to 1 in order to be consistent with DFT calculation. The dependence of polarization on electric field cycling is shown in Figure 6a. It is found that increasing oxygen vacancy concentration not only widens the loop but also greatly enhances the remnant polarization, indicating the possibility to improve ferroelectricity by tuning oxygen vacancy concentration. Inspired by theoretical prediction, the (001) $(STO)_9/(SRO)_1$ superlattice were experimentally fabricated by pulsed laser deposition on a (001)-oriented Nb-doped STO substrate (for detail see Methods). The polarization vs. hysteresis (*P*–*E*) loops were measured by standard ferroelectric testing system (TF2000E; Aixacct, Aachen, Germany). As shown in Figure 6b, a stable and switchable polarization is indeed observed in $(STO)_9/(SRO)_1$ superlattices. The films exhibited an evident polarization hysteresis with a remnant polarization of 8 $\mu C/cm^2$. In contrast, pure STO film showed linear polarization response, indicating a paraelectric behavior. We note that the observed polarization value in the experimentally grown films is

smaller than the theoretically predicted value. This could result from the lower oxygen vacancy concentration in the experimentally grown films due to high oxygen partial pressure during growth (see Methods). The polarization can be enhanced by increasing the oxygen vacancy concentration by post annealing or electroforming. It should be noted that the pronounced ferroelectric response of $(STO)_9/(SRO)_1$ superlattices requires a forming process by electric field cycling in experiment. The electroforming process may originate from the redistribution of oxygen vacancies at interface after a multiple electric cycling as illustrated by our KMC simulation in Figure 5. According to the relation of $D_V = D_V^0 \exp(-H/kT)$, where D_V is oxygen vacancy diffusion coefficient and H is diffusion barrier, the oxygen vacancy can move more easily at higher temperature due to thermal activation in STO.[65] Therefore, the $P-E$ loop will be strongly impacted by temperature. The effect of temperature on $P-E$ hysteresis loops of $(STO)_9/(SRO)_1$ superlattices is shown in Figure S8. The shape of hysteresis loops did not change as temperature was changed from 30 to 60 ^oC. However, the hysteresis loop subsided and became linear as temperature was raised to 80 ^oC. The linear P-E loop at high temperature likely arises from release of oxygen vacancy at high temperature and is consistent with predicted non-ferroelectricity behavior in oxygen-vacancy free supercell as shown in Figure 2c. It suggests that once the oxygen vacancies diminish, the superlattice cannot maintain the non-volatility. What is more, the ferroelectricity did not recover when sample was cooled back to room temperature, further implying the oxygen vacancy release mechanism. Our measurements of $P-E$ hysteresis confirm the ferroelectricity in $(STO)_9/(SRO)_1$ heterostructures.

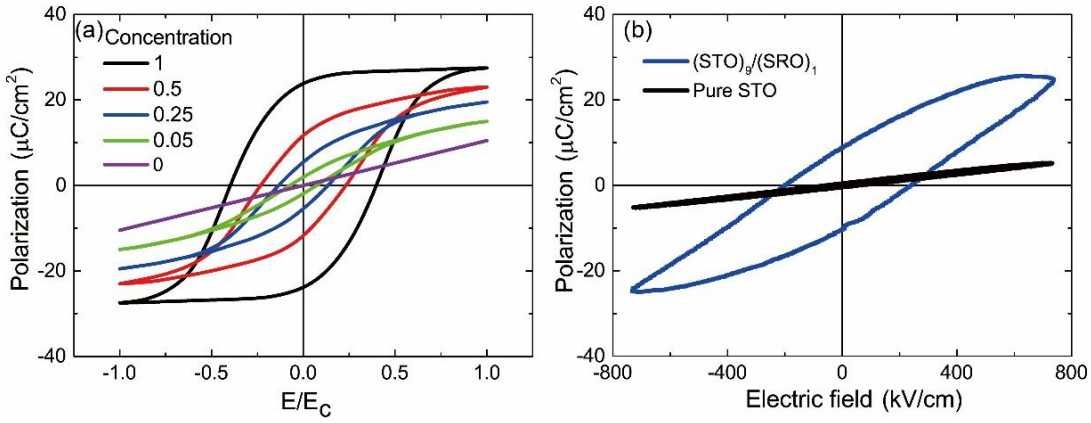

Figure 6. (a) Simulated *P*−*E* hysteresis loop for different concentration of the interfacial oxygen vacancy by Landau Ginzburg-Devonshire phenomenological theory calculation. (b) *P*−*E* hysteresis loop of the experimentally grown pure STO film and the $(STO)_9/(SRO)_1$ superlattices.

4. Conclusions

In conclusion, our study demonstrates a realization of strong ferroelectricity in oxide heterostructure comprised of otherwise non-ferroelectric $SrTiO_3$ and $SrRuO_3$ through interface oxygen vacancies-controlled inversion symmetry breaking. A desired oxygen vacancies favorite sites and migration behaviors across interfaces are obtained by designing profile of oxygen vacancies formation energy and diffusion barrier. This well controlled oxygen vacancies at interface leads to surprisingly significant ferroelectricity, which can be enhanced by increasing oxygen vacancies concentration. Besides, it can be significantly enhanced by reducing STO thickness, in strong contrast to other conventional ferroelectric oxides where ferroelectricity subsides with reducing thickness.

Usually, the vacancies can occupy different atomic sites in oxide heterostructures and thus their disordering structure is detrimental to inversion symmetry breaking, slowing down the discovery of new materials by defect engineered symmetry breaking. Our proposed route to achieve desired oxygen vacancies profile and migration channel can be extended to many other perovskite heterostructures. What is more, this defect-engineered symmetry breaking paves a path toward electronic devices in which ferroelectricity is coupled to other symmetry-related functional properties, such as superconductivity, magnetism, and Rashba spin splitting.

Supporting Information

Group theory analysis; point group of superlattice when oxygen vacancy in different position(Table S1); DFT calculations of Ti atoms shift off the center of pseudo-cubic unit cell displacement (Figure S1); The effect of strain on polarization in the superlattices (Figure S2); oxygen vacancy concentration and STO thickness dependent polarization (Figure S3 and S4); polarization of $(LaAlO_3)_9/(LaNiO_3)_1$ superlattice with oxygen vacancy (Figure S5); formation energy of different arrangements of divacancies (Figure S6); the polarization of superlattice with oxygen vacancies are distributed at two symmetrical interfaces (Figure S7); *P*−*E* hysteresis loops of the STO/SRO superlattice measured at different temperatures (Figure S8).

ACKNOWLEDGMENTS

This work was supported by the National Key R&D Program of China (Grant No. 2017YFA0303602), the National Nature Science Foundation of China (Grants No. 11774360, No. 11974365, and No. 51931011), and Key Research Program of Frontier Sciences, CAS (No. ZDBS-LY-SLH008). Research by Z.L. was financially supported by Hundred Talent Program of the Chinese Academy of Sciences (Grant no. KJ2310000010), National Nature Science Foundation of China (Grants no. 11974325) and Collaborative Innovation Program of Hefei Science Center, CAS (Grants no. 2019HSC-CIP008). The authors are thankful for the computational resources at Supercomputing Center of Ningbo Institute of Materials Technology and Engineering.

References

1. Wang, Z.; Guo, H.; Shao, S.; Saghayezhian, M.; Li, J.; Fittipaldi, R.; Vecchione, A.; Siwakoti, P.; Zhu, Y.; Zhang, J.; Plummer, E. W. Designing Antiphase Boundaries by Atomic Control of Heterointerfaces. *Proc. Natl. Acad. Sci.* **2018,** 115, 9485-9490.

2. Park, J. S.; Kim, S.; Xie, Z.; Walsh, A. Point Defect Engineering in Thin-film Solar Cells. *Nat. Rev. Mater.* **2018,** 3, 194-210.

3. Qin, M.; Gao, F.; Cizek, J.; Yang, S.; Fan, X.; Zhao, L.; Xu, J.; Dong, G.; Reece, M.; Yan, H. Point Defect Structure of La-Doped $SrTiO_3$ Ceramics with Colossal Permittivity. *Acta Mater.* **2019,** 164, 76-89.

4. Hu, L.; Zhu, T.; Liu, X.; Zhao, X. Point Defect Engineering of High-Performance Bismuth-Telluride-Based Thermoelectric Materials. *Adv. Funct. Mater.* **2014,** 24, 5211-5218.

5. Pantelides, S. T. The Electronic Structure of Impurities and other Point Defects in Semiconductors. *Rev. Mod. Phys.* **1978,** 50, 797-858.

6. Stoneham, A. M.; Smoluchowski, R. Theory of Defects in Solids: Electronic Structure of Defects in Insulators and Semiconductors. *Phys. Today* **1976,** 29, 62-62.

7. Tranquada, J. M.; Heald, S. M.; Moodenbaugh, A. R.; Liang, G.; Croft, M. Nature of the Charge Carriers in Electron-Doped Copper Oxide Superconductors. *Nature* **1989,** 337, 720-721.

8. Takagi, H.; Uchida, S.; Tokura, Y. Superconductivity Produced by Electron Doping in CuO_2-Layered Compounds. *Phys. Rev. Lett.* **1989,** 62, 1197-1200.

9. Zhang, H.; Wang, Y. Y.; Zhang, H.; Dravid, V. P.; Marks, L. D.; Han, P. D.; Payne, D. A.; Radaelli, P. G.; Jorgensen, J. D. Identity of Planar Defects in the Infinite-Layer Copper Oxide Superconductor. *Nature* **1994,** 370, 352-354.

10. Urushibara, A.; Moritomo, Y.; Arima, T.; Asamitsu, A.; Kido, G.; Tokura, Y. Insulator-Metal Transition and Giant Magnetoresistance in $La_{1-x}Sr_xMnO_3$. *Phys. Rev. B* **1995,** 51, 14103-14109.

11. Röder, H.; Zang, J.; Bishop, A. R. Lattice Effects in the Colossal-Magnetoresistance Manganites. *Phys. Rev. Lett.* **1996,** 76, 1356-1359.

12. Shi, J.; Zhou, Y.; Ramanathan, S. Colossal Resistance Switching and Band Gap Modulation in a Perovskite Nickelate by Electron Doping. *Nat. Commun.* **2014,** 5, 4860.

13. Scherwitzl, R.; Zubko, P.; Lezama, I. G.; Ono, S.; Morpurgo, A. F.; Catalan, G.; Triscone, J.-M. Electric-Field Control of the Metal-Insulator Transition in Ultrathin $NdNiO_3$ Films. *Adv. Mater.* **2010,** 22, 5517-5520.

14. Wang, L.; Dash, S.; Chang, L.; You, L.; Feng, Y.; He, X.; Jin, K.-j.; Zhou, Y.; Ong, H. G.; Ren, P.; Wang, S.; Chen, L.; Wang, J. Oxygen Vacancy Induced Room-Temperature Metal-Insulator Transition in Nickelate Films and Its Potential Application in Photovoltaics. *ACS Appl. Mater. Interfaces* **2016,** 8, 9769-9776.

15. Bartram, R. H., *Symmetry of Point Imperfections in Solids*. in *Symmetry*. Elsevier: 1986. 185-196.

16. Michel, L. Symmetry Defects and Broken Symmetry Configurations Hidden Symmetry. *Rev. Mod. Phys.* **1980,** 52, 617-651.

17. Gong, X.; Kargarian, M.; Stern, A.; Yue, D.; Zhou, H.; Jin, X.; Galitski, V. M.; Yakovenko, V. M.; Xia, J. Time-Reversal Symmetry-Breaking Superconductivity in Epitaxial Bismuth/Nickel Bilayers. *Sci. Adv.* **2017,** 3, e1602579.

18. Yu, Y.; Ma, L.; Cai, P.; Zhong, R.; Ye, C.; Shen, J.; Gu, G. D.; Chen, X. H.; Zhang, Y. High-Temperature Superconductivity in Monolayer $Bi_2Sr_2CaCu_2O_{8+\delta}$. *Nature* **2019**, 575, 156-163.

19. Hinojosa, A.; Fernandes, R. M.; Chubukov, A. V. Time-Reversal Symmetry Breaking Superconductivity in the Coexistence Phase with Magnetism in Fe Pnictides. *Phys. Rev. Lett.* **2014,** 113, 167001.

20. Sunko, V.; Rosner, H.; Kushwaha, P.; Khim, S.; Mazzola, F.; Bawden, L.; Clark, O. J.; Riley, J. M.; Kasinathan, D.; Haverkort, M. W.; Kim, T. K.; Hoesch, M.; Fujii, J.; Vobornik, I.; Mackenzie, A. P.; King, P. D. C. Maximal Rashba-Like Spin Splitting via Kinetic-Energy-Coupled Inversion-Symmetry Breaking. *Nature* **2017,** 549, 492-496.

21. Cho, J.; Kim, N.-H.; Lee, S.; Kim, J.-S.; Lavrijsen, R.; Solignac, A.; Yin, Y.; Han, D.-S.; van Hoof, N. J. J.; Swagten, H. J. M.; Koopmans, B.; You, C.-Y. Thickness Dependence of the Interfacial Dzyaloshinskii-Moriya Interaction in Inversion Symmetry Broken Systems. *Nat. Commun.* **2015,** 6, 7635.

22. Zhang, X.; Liu, Q.; Luo, J.-W.; Freeman, A. J.; Zunger, A. Hidden Spin Polarization in Inversion-Symmetric Bulk Crystals. *Nat. Phys.* **2014,** 10, 387-393.

23. Kolpak, A. M.; Walker, F. J.; Reiner, J. W.; Segal, Y.; Su, D.; Sawicki, M. S.; Broadbridge, C. C.; Zhang, Z.; Zhu, Y.; Ahn, C. H.; Ismail-Beigi, S. Interface-Induced Polarization and Inhibition of Ferroelectricity in Epitaxial $SrTiO_3$/Si. *Phys. Rev. Lett.* **2010,** 105, 217601.

24. Newnham, R. E., *Properties of Materials: Anisotropy, Symmetry, Structure*. Oxford University

Press on Demand: 2005.

25. Eason, R., *Pulsed Laser Deposition of Thin Films: Applications-Led Growth of Functional Materials*. John Wiley & Sons: 2007.

26. Eckstein, J. N.; Bozovic, I. High-Temperature Superconducting Multilayers and Heterostructures Grown by Atomic Layer-by-Layer Molecular Beam Epitaxy. *Annu. Rev. Mater. Sci.* **1995,** 25, 679-709.

27. Nie, Y.; Zhu, Y.; Lee, C.-H.; Kourkoutis, L. F.; Mundy, J. A.; Junquera, J.; Ghosez, P.; Baek, D.; Sung, S.; Xi, X. Atomically Precise Interfaces from Non-Stoichiometric Deposition. *Nat. Commun.* **2014,** 5, 4530.

28. Zhang, L.; Bredeson, I.; Birenbaum, A. Y.; Kent, P. R.; Cooper, V. R.; Ganesh, P.; Xu, H. Oxygen Vacancy Formation Energies in $PbTiO_3/SrTiO_3$ Superlattice. *Nat. Rev. Mater* **2018,** 2, 064409.

29. Park, C. H.; Chadi, D. J. Microscopic Study of Oxygen-Vacancy Defects in Ferroelectric Perovskites. *Phys. Rev. B* **1998,** 57, R13961-R13964.

30. Evarestov, R. A.; Gryaznov, D.; Arrigoni, M.; Kotomin, E. A.; Chesnokov, A.; Maier, J. Use of Site Symmetry in Supercell Models of Defective Crystals: Polarons in CeO_2. *Phys. Chem. Chem. Phys.* **2017,** 19, 8340-8348.

31. Muller, D. A.; Nakagawa, N.; Ohtomo, A.; Grazul, J. L.; Hwang, H. Y. Atomic-Scale Imaging of Nanoengineered Oxygen Vacancy Profiles in SrTiO3. *Nature* **2004,** 430, 657-661.

32. Kresse, G.; Furthmüller, J. Efficiency of Ab-Initio Total Energy Calculations for Metals and Semiconductors using a Plane-Wave Basis Set. *Comput. Mater. Sci.* **1996,** 6, 15-50.

33. Kresse, G.; Furthmüller, J. Efficient Iterative Schemes for Ab Initio Total-Energy Calculations using a Plane-Wave Basis Set. *Phys. Rev. B* **1996,** 54, 11169-11186.

34. Perdew, J. P.; Ruzsinszky, A.; Csonka, G. I.; Vydrov, O. A.; Scuseria, G. E.; Constantin, L. A.; Zhou, X.; Burke, K. Restoring the Density-Gradient Expansion for Exchange in Solids and Surfaces. *Phys. Rev. Lett.* **2008,** 100, 136406.

35. Pan, F.; Yin, S.; Subramanian, V. A Detailed Study of the Forming Stage of an Electrochemical Resistive Switching Memory by KMC Simulation. *IEEE Electron Device Lett.* **2011,** 32, 949-951.

36. Li, D.; Li, M.; Zahid, F.; Wang, J.; Guo, H. Oxygen Vacancy Filament Formation in TiO_2: a Kinetic Monte Carlo Study. *J. Appl. Phys.* **2012,** 112, 073512.

37. Glinchuk, M. D.; Morozovska, A. N.; Lukowiak, A.; Stręk, W.; Silibin, M. V.; Karpinsky, D. V.; Kim, Y.; Kalinin, S. V. Possible Electrochemical Origin of Ferroelectricity in HfO_2 Thin Films. *J. Alloy. Compd.* **2020**, 153628.

38. Lytle, F. W. X-Ray Diffractometry of Low-Temperature Phase Transformations in Strontium Titanate. *J. Appl. Phys.* **1964,** 35, 2212-2215.

39. Müller, K. A.; Burkard, H. $SrTiO_3$: An Intrinsic Quantum Paraelectric Below 4 K. *Phys. Rev. B* **1979,** 19, 3593-3602.

40. Wang, Q.-Y.; Li, Z.; Zhang, W.-H.; Zhang, Z.-C.; Zhang, J.-S.; Li, W.; Ding, H.; Ou, Y.-B.; Deng, P.; Chang, K.; Wen, J.; Song, C.-L.; He, K.; Jia, J.-F.; Ji, S.-H.; Wang, Y.-Y.; Wang, L.-L.; Chen, X.; Ma, X.-C.; Xue, Q.-K. Interface-Induced High-Temperature Superconductivity in Single Unit-Cell FeSe Films on $SrTiO_3$. *Chin. Phys. Lett.* **2012,** 29, 037402.

41. Cuong, D. D.; Lee, B.; Choi, K. M.; Ahn, H.-S.; Han, S.; Lee, J. Oxygen Vacancy Clustering and Electron Localization in Oxygen-Deficient $SrTiO_3$ LDA+U Study. *Phys. Rev. Lett.* **2007,** 98, 115503.

42. Pavlenko, N.; Kopp, T.; Tsymbal, E. Y.; Mannhart, J.; Sawatzky, G. A. Oxygen Vacancies at Titanate Interfaces: Two-Dimensional Magnetism and Orbital Reconstruction. *Phys. Rev. B* **2012,** 86, 064431.

43. Lopez-Bezanilla, A.; Ganesh, P.; Littlewood, P. B. Magnetism and Metal-Insulator Transition in Oxygen-Deficient $SrTiO_3$. *Phys. Rev. B* **2015,** 92, 115112.

44. Koster, G.; Klein, L.; Siemons, W.; Rijnders, G.; Dodge, J. S.; Eom, C.-B.; Blank, D. H. A.; Beasley, M. R. Structure, Physical Properties, and Applications of $SrRuO_3$ Thin Films. *Rev. Mod. Phys.* **2012,** 84, 253-298.

45. Shieh, J.; Yeh, J. H.; Shu, Y. C.; Yen, J. H. Hysteresis Behaviors of Barium Titanate Single Crystals Based on the Operation of Multiple 90° Switching Systems. *Mater. Sci. Eng. B* **2009,** 161, 50-54.

46. Haeni, J. H.; Irvin, P.; Chang, W.; Uecker, R.; Reiche, P.; Li, Y. L.; Choudhury, S.; Tian, W.; Hawley, M. E.; Craigo, B.; Tagantsev, A. K.; Pan, X. Q.; Streiffer, S. K.; Chen, L. Q.; Kirchoefer, S. W.; Levy, J.; Schlom, D. G. Room-Temperature Ferroelectricity in Strained $SrTiO_3$. *Nature* **2004,** 430, 758-761.

47. Nazir, S.; Cheng, J.; Yang, K. Creating Two-Dimensional Electron Gas in Nonpolar/Nonpolar Oxide Interface via Polarization Discontinuity: First-Principles Analysis of $CaZrO_3/SrTiO_3$ Heterostructure. *ACS Appl. Mater. Interfaces* **2016,** 8, 390-399.

48. Chen, Y.; Trier, F.; Kasama, T.; Christensen, D. V.; Bovet, N.; Balogh, Z. I.; Li, H.; Thydén, K. T. S.; Zhang, W.; Yazdi, S.; Norby, P.; Pryds, N.; Linderoth, S. Creation of High Mobility Two-Dimensional Electron Gases via Strain Induced Polarization at an Otherwise Nonpolar Complex Oxide Interface. *Nano Lett.* **2015,** 15, 1849-1854.

49. Reyes-Lillo, S. E.; Rabe, K. M.; Neaton, J. B. Ferroelectricity in [111]-Oriented Epitaxially Strained $SrTiO_3$ From First Principles. *Phys. Rev. Mater.* **2019,** 3, 030601.

50. Pertsev, N. A.; Tagantsev, A. K.; Setter, N. Phase Transitions and Strain-Induced Ferroelectricity in $SrTiO_3$ Epitaxial Thin Films. *Phys. Rev. B* **2000,** 61, R825-R829.

51. Kalabukhov, A.; Gunnarsson, R.; Börjesson, J.; Olsson, E.; Claeson, T.; Winkler, D. Effect of Oxygen Vacancies in the $SrTiO_3$ Substrate on the Electrical Properties of the $LaAlO_3/SrTiO_3$ Interface. *Phys. Rev. B* **2007,** 75, 121404.

52. Junquera, J.; Ghosez, P. Critical Thickness for Ferroelectricity in Perovskite Ultrathin Films. *Nature* **2003,** 422, 506-509.

53. Gerra, G.; Tagantsev, A. K.; Setter, N.; Parlinski, K. Ionic Polarizability of Conductive Metal Oxides and Critical Thickness for Ferroelectricity in $BaTiO_3$. *Phys. Rev. Lett.* **2006,** 96, 107603.

54. Kim, Y. S.; Kim, D. H.; Kim, J. D.; Chang, Y. J.; Noh, T. W.; Kong, J. H.; Char, K.; Park, Y. D.; Bu, S. D.; Yoon, J.-G.; Chung, J.-S. Critical Thickness of Ultrathin Ferroelectric $BaTiO_3$ Films. *Appl. Phys. Lett.* **2005,** 86, 102907.

55. Shin, Y. J.; Kim, Y.; Kang, S.-J.; Nahm, H.-H.; Murugavel, P.; Kim, J. R.; Cho, M. R.; Wang, L.; Yang, S. M.; Yoon, J.-G.; Chung, J.-S.; Kim, M.; Zhou, H.; Chang, S. H.; Noh, T. W. Interface Control of Ferroelectricity in an $SrRuO_3/BaTiO_3/SrRuO_3$ Capacitor and its Critical Thickness. *Adv. Mater.* **2017,** 29, 1602795.

56. Stengel, M.; Vanderbilt, D.; Spaldin, N. A. Enhancement of Ferroelectricity at Metal-Oxide Interfaces. *Nat. Mater.* **2009,** 8, 392-397.

57. Lee, S. R.; Baasandorj, L.; Chang, J. W.; Hwang, I. W.; Kim, J. R.; Kim, J.-G.; Ko, K.-T.; Shim, S. B.; Choi, M. W.; You, M.; Yang, C.-H.; Kim, J.; Song, J. First Observation of Ferroelectricity in ~1 nm Ultrathin Semiconducting $BaTiO_3$ Films. *Nano Lett.* **2019,** 19, 2243-2250.

58. Cheema, S. S.; Kwon, D.; Shanker, N.; dos Reis, R.; Hsu, S.-L.; Xiao, J.; Zhang, H.; Wagner, R.; Datar, A.; McCarter, M. R.; Serrao, C. R.; Yadav, A. K.; Karbasian, G.; Hsu, C.-H.; Tan, A. J.; Wang, L.-C.; Thakare, V.; Zhang, X.; Mehta, A.; Karapetrova, E.; Chopdekar, R. V.; Shafer, P.; Arenholz, E.;

Hu, C.; Proksch, R.; Ramesh, R.; Ciston, J.; Salahuddin, S. Enhanced Ferroelectricity in Ultrathin Films Grown Directly on Silicon. *Nature* **2020,** 580, 478-482.

59. Lee, H.-J.; Lee, M.; Lee, K.; Jo, J.; Yang, H.; Kim, Y.; Chae, S. C.; Waghmare, U.; Lee, J. H. Scale-Free Ferroelectricity induced by Flat Phonon Bands in HfO_2. *Science* **2020**, eaba0067.

60. Starschich, S.; Menzel, S.; Böttger, U. Evidence for Oxygen Vacancies Movement during Wake-Up in Ferroelectric Hafnium Oxide. *Appl. Phys. Lett.* **2016,** 108, 032903.

61. Zhou, Y.; Zhang, Y. K.; Yang, Q.; Jiang, J.; Fan, P.; Liao, M.; Zhou, Y. C. The Effects of Oxygen Vacancies on Ferroelectric Phase Transition of HfO_2-Based Thin Film from First-Principle. *Comput. Mater. Sci.* **2019,** 167, 143-150.

62. Kolodiazhnyi, T.; Tachibana, M.; Kawaji, H.; Hwang, J.; Takayama-Muromachi, E. Persistence of Ferroelectricity in $BaTiO_3$ through the Insulator-Metal Transition. *Phys. Rev. Lett.* **2010,** 104, 147602.

63. Hu, L.; Luo, X.; Zhang, K. J.; Tang, X. W.; Zu, L.; Kan, X. C.; Chen, L.; Zhu, X. B.; Song, W. H.; Dai, J. M.; Sun, Y. P. Oxygen Vacancies-Induced Metal-Insulator Transition in $La_{2/3}Sr_{1/3}VO_3$ Thin Films: Role of the Oxygen Substrate-to-Film Transfer. *Appl. Phys. Lett.* **2014,** 105, 111607.

64. Zhuang, H. L.; Ganesh, P.; Cooper, V. R.; Xu, H.; Kent, P. R. C. Understanding the Interactions between Oxygen Vacancies at $SrTiO_3$ (001) Surfaces. *Phys. Rev. B* **2014,** 90, 064106.

65. De Souza, R. A.; Metlenko, V.; Park, D.; Weirich, T. E. Behavior of Oxygen Vacancies in Single-Crystal $SrTiO_3$: Equilibrium Distribution and Diffusion Kinetics. *Phys. Rev. B* **2012,** 85, 174109.

66. De Souza, R. A. Oxygen Diffusion in $SrTiO_3$ and Related Perovskite Oxides. *Adv. Funct. Mater.* **2015,** 25, 6326-6342.

67. Schraknepper, H.; Bäumer, C.; Dittmann, R.; De Souza, R. A. Complex Behaviour of Vacancy Point-Defects in $SrRuO_3$ Thin Films. *Phys. Chem. Chem. Phys.* **2015,** 17, 1060-1069.

68. Lu, J.; Si, L.; Yao, X.; Tian, C.; Wang, J.; Zhang, Q.; Lai, Z.; Malik, I. A.; Liu, X.; Jiang, P.; Zhu, K.; Shi, Y.; Luo, Z.; Gu, L.; Held, K.; Mi, W.; Zhong, Z.; Nan, C.-W.; Zhang, J. Electric Field Controllable High-Spin $SrRuO_3$ Driven by a Solid Ionic Junction. *Phys. Rev. B* **2020,** 101, 214401.

69. Bark, C. W.; Sharma, P.; Wang, Y.; Baek, S. H.; Lee, S.; Ryu, S.; Folkman, C. M.; Paudel, T. R.; Kumar, A.; Kalinin, S. V.; Sokolov, A.; Tsymbal, E. Y.; Rzchowski, M. S.; Gruverman, A.; Eom, C. B. Switchable Induced Polarization in $LaAlO_3/SrTiO_3$ Heterostructures. *Nano Lett.* **2012,** 12, 1765-1771.

70. Xue, W.; Liu, G.; Zhong, Z.; Dai, Y.; Shang, J.; Liu, Y.; Yang, H.; Yi, X.; Tan, H.; Pan, L.; Gao, S.; Ding, J.; Xu, X.-H.; Li, R.-W. A 1D Vanadium Dioxide Nanochannel Constructed via Electric-Field-Induced Ion Transport and Its Superior Metal-Insulator Transition. *Adv. Mater.* **2017,** 29, 1702162.

71. Lu, N.; Zhang, P.; Zhang, Q.; Qiao, R.; He, Q.; Li, H.-B.; Wang, Y.; Guo, J.; Zhang, D.; Duan, Z.; Li, Z.; Wang, M.; Yang, S.; Yan, M.; Arenholz, E.; Zhou, S.; Yang, W.; Gu, L.; Nan, C.-W.; Wu, J.; Tokura, Y.; Yu, P. Electric-Field Control of Tri-State Phase Transformation with a Selective Dual-Ion Switch. *Nature* **2017,** 546, 124-128.

72. Shibuya, K.; Dittmann, R.; Mi, S.; Waser, R. Impact of Defect Distribution on Resistive Switching Characteristics of Sr_2TiO_4 Thin Films. *Adv. Mater.* **2010,** 22, 411-414.

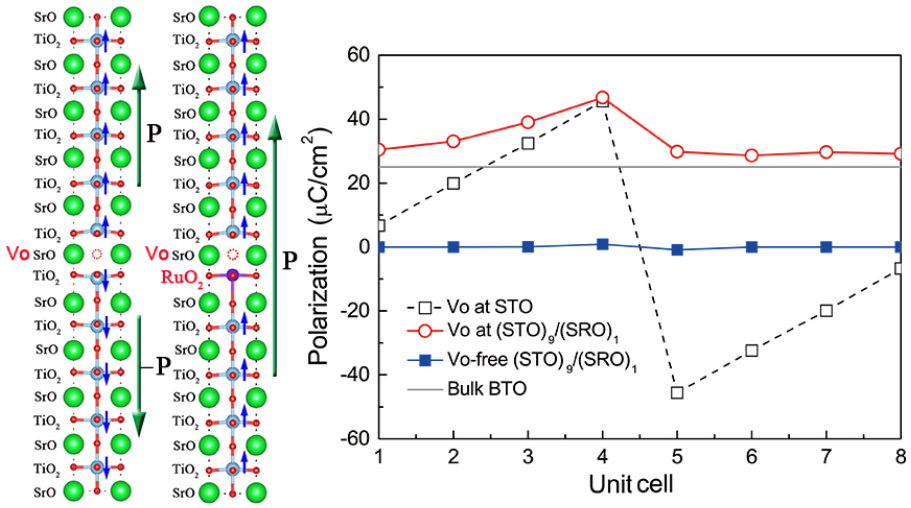

Table of Contents Graphic